Turbulence, Heat and Mass Transfer 8

Heat Transfer Characteristics of Viscoelastic Fluid in Transitional Flow through a Serpentine Channel

K. Tatsumi, R. Kimura, N. Shinotsuka and K. Nakabe

[1]*Departiment of Mechanical Engineering and Science, Kyoto University, Kyotodaigakukatsura, 615-8540 Kyoto, Japan, tatsumi@me.kyoto-u.ac.jp*

Abstract – The local heat transfer, pressure loss and flow characteristics of the viscoelastic fluid in the transition and developed flows through a serpentine channel are described in this study. The flows became unsteady and longitudinal vortices-like secondary flows were generated even under low Reynolds number condition of Re~1 due to the normal stress differences produced by the viscoelasticity of the fluid. This enhanced the heat transfer performance markedly. The vortex structures changed depending on the streamwise position and Weissenberg number and showed three transition stages: a pair of moderate vortices, a single vortex with a drift of main flow toward the wall, and a pair of strong vortices. These vortices affected the local heat transfer characteristics at the top-bottom walls and sidewalls, their streamwise distributions and their unsteady behavior.

1. Introduction

Viscoelastic fluid produces interesting and effective flow structures and features from physical and industrial point of view in various channels and condition. The viscoelasticity of the fluid can provide an increase of the flow instability and generate unsteady flows under low Reynolds number conditions. It can also generate secondary flows due to the appearance of the normal stress differences which accompanies important transport phenomena as enhancement of fluid mixing and heat transfer at the channel walls.

The influences of the rheological properties of the viscoelastic fluid on laminar heat transfer have been keenly studied in the past several decades for various channel flows. Chunbo & Hartnett (1992) reported that the heat transfer coefficient in the case of viscoelastic fluid flow in straight channels was higher than the Newtonian fluid case. The main cause was attributed to the secondary flow which was generated and enhanced by the normal stress difference. Recently, several studies have shown that unsteady flow is observed in viscoelastic fluid of flows through a serpentine channel and good mixing can be achieved even under low Reynolds number conditions of Re<10 [3-6].

The authors have carried out measurements of average heat transfer coefficients, pressure losses and flow velocities of viscoelastic fluid in low Reynolds number (Re~1) flows through a serpentine channel [7, 8]. The influence of the fluid properties on these characteristics was evaluated to understand the correlations of dimensionless fluid parameters. Effective secondary flows were generated accompanying remarkable enhancement in the heat transfer with a reasonable pressure loss increase. However, a full understanding of the relationship between the vortices and heat transfer characteristics remains as a problem to be solved.

In this study, flow visualization and measurement of local heat transfer coefficient are carried out for flow in a channel expanded in the streamwise direction. The influences of the local positions, flow conditions including the developing and developed regions, and the fluid viscoelastic properties on the relationships between the flow structure and heat transfer characteristics are discussed to understand the mechanism of heat transfer enhancement.

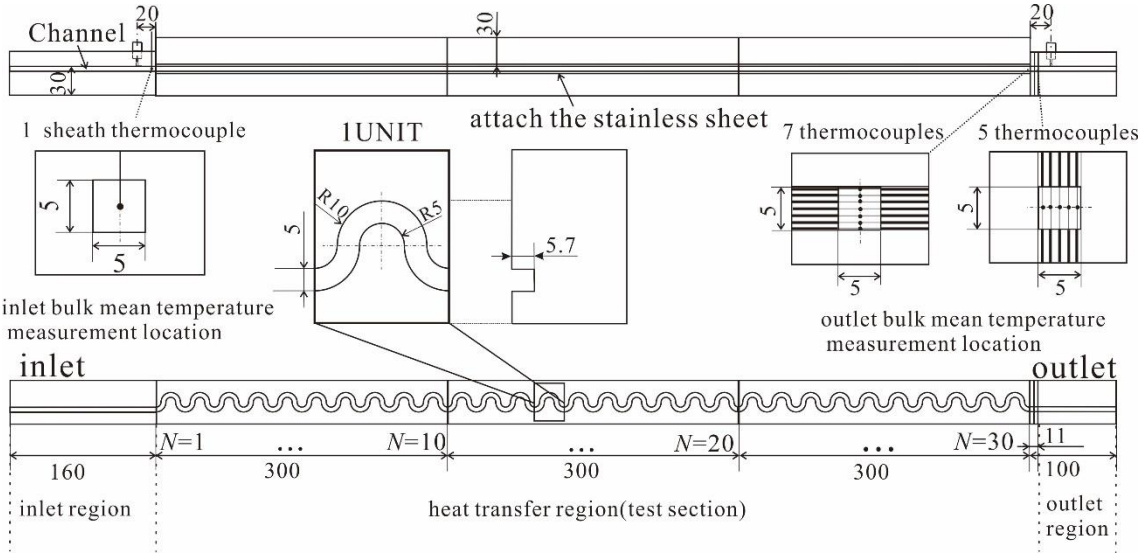

Figure 1: Experimental apparatus of the heat transfer and pressure loss measurements of flows in a serpentine channel.

2. Experimental Methods

Fig. 1 shows the experimental apparatus and the serpentine channel of the present study. The serpentine channel had a square cross section 5 mm on a side, and consists of semicircle parts connected periodically in the streamwise direction. The inner and outer radii of the semicircle part were R_i = 5mm and R_o = 10mm, respectively. To evaluate the heat transfer characteristics in the transitional flow and developed flow regions, the number of the curve units, N, were set as 30.

Constant heat flux conditions were applied to the channel walls in the heat transfer measurements. Stainless steel films with thickness of 0.5mm were attached to the walls to which direct current was supplied. The wall temperatures were measured by attaching thermocouples to the stainless steel from the backside taking account of the heat and electric insulations. Two test sections, one with the top and bottom walls heated, and the other with sidewalls heated were employed in this study. The unheated walls were designed to be transparent in order to perform the flow visualization through these walls simultaneously with the heat transfer measurement.

The bulk mean temperatures of the fluid at the inlet and outlet of the test section were obtained using the fluid temperatures measured at each location. At the inlet a sheath-type thermocouple was inserted to measure the fluid temperature at the center of the cross-section. At the outlet, 5 and 7 thermocouples were placed with equal space in the spanwise and height directions, respectively. Fully developed velocity profile of a square channel was applied to these temperature to calculate the bulk mean temperature.

The heat transfer coefficients were calculated by the local heat flux, wall temperature T_w and the local bulk mean temperature $T_{m,x}$. $T_{m,x}$ of each streamwise position and the wall heat flux q_w can be estimated from the voltage and current applied to the heating plate, and the inlet and outlet bulk mean temperatures. However, due to considerable effects of the heat conduction in the streamwise direction and heat loss to the surrounding walls appearing under the low Reynolds number conditions, three-dimensional numerical simulation was performed using the authors' original code to calculate $T_{m,x}$ and q_w.

As mentioned previously, flow visualization using dye was carried out simultaneously with the heat transfer measurement to understand the flow behavior in the channel. A syringe needle

with a pore located at the side of its end was inserted from the sidewalls of the channel of which the top and bottom walls were heated. Working fluid to which blue ink was added by 2wt%, was supplied to the channel through the needle by a syringe pump (Harvard Apparatus: econoflo). The images of the streak lines were recorded using a digital video camera (Sony: HDR-CX370V) measured from the side walls of the channel.

Pressure loss was measured by two pressure gauges installed to the inlet and outlet of the test section as shown in Fig. 1.

The working fluid was supplied from a pressurized tank to the channel without using any mechanical pump to avoid flow fluctuation. The mass of the fluid flowing from the outlet was measured by an electronic balance to measure the mass flow rate.

An aqueous solution of 500ppm polyacrylamide (PAAm, MW: 1.8×10^7), 1wt% NaCl, and 64.4wt% sucrose was used as viscoelastic fluids. Sucrose was mixed in the fluid to mainly increase the viscosity of the solution. NaCl was added as a counter ion to prevent the shear thinning effects and the aggregation of the polymers. An aqueous solution of 64.4wt% sucrose only was used as Newtonian fluids to compare with the viscoelastic fluids. The fluid viscosity and relaxation time were measured by a rheometer in advance of the experiment to define the following dimensionless values.

The sucrose concentration in the PAAm solution is changed to evaluate the effects of the physical properties particularly the viscoelasticity on the heat transfer characteristics. In this case, solutions of three concentration conditions, i.e. 64.4, 60.0 and 57.0wt%, were prepared and measured.

The range of the flow conditions are summarized in Table 1. The parenthetic values of the PAAm presents the sucrose concentration. The definition of the values are Reynolds number $Re=\rho U_m D_h/\mu$, Dean number, $N_D=\mathrm{Re}\sqrt{D_h/2r}$ and Weissenberg number, $Wi=4\lambda U_m/D_h$, respectively. U_m and D_h are the cross-sectional average velocity and the hydraulic diameter. ρ, μ and λ are the density, viscosity and relaxation time of the solution. *Pr* is the Prandtl number.

Table 1: Experimental conditions and dimensionless values.

Fluid	U_m [mm/s]	*Re*	*Pr*	N_D	*Wi*
PAAm(64)	4.6–77.4	0.1–1.8	1280–2470	0.1–1.1	8–220
Sucrose	5.1–29.8	0.6–2.1	420–650	0.3–1.2	–

As previously mentioned, the rheological properties of the working fluid are measured using a rheometer (Anton Paar: MCR-301). The effects of temperature and shear rate on the viscosity μ and relaxation time λ were evaluated by applying the Kampmeyer-Girifalco equation (modified version of Andrade and Guzman equation) [9, 10] to the relationship between the viscosity and temperature, and the shear rate as shown in Equations (1) and (2).

$$\mu = K\mu\dot{\gamma}^{n-1} \tag{1}$$

$$\log_{10}\mu(\dot{\gamma}_m, T_m) = \alpha(\dot{\gamma}_m) + \frac{\beta}{T_m+273} + \frac{\varepsilon}{(T_m+273)^2} \tag{2}$$

Shear rate is calculated as $\dot{\gamma}=4U_m/D_h$. β and ε are constants which were obtained by the measurement carried out under the condition of T_m=20°C. These two values were not largely influenced by the temperature, and was used as constants for other temperature conditions. As for α which is dependent with the shear rate, the value was obtained using Eq. (3), in which the

values of T_m=20°C was also applied.

$$\alpha(\dot{\gamma}_m) = \log_{10}\left(K_{m,20}\dot{\gamma}_m^{n-1}\right) - \left(\frac{\beta}{T_{20}+273} + \frac{\varepsilon}{(T_{20}+273)^2}\right) \tag{3}$$

The coefficients are summarized in Table 2.

Table 2: Coefficients used to define the viscosity and relaxation times.

Fluid	$K\mu$	n	β	ε
PAAm(64)	0.54	0.86	-3.1×10^3	8.0×10^5
PAAm(60)	0.29	0.85	-3.6×10^3	8.0×10^5
PAAm(57)	0.20	0.83	-3.8×10^3	8.0×10^5
Sucrose	0.13	1	-3.1×10^3	8.0×10^5

The relaxation time was measured by applying the general Maxwell model (Eq. (4)) to the time distribution of the shear stress observed after loading a step pattern stress to the fluid.

$$\tau = \sum_{i=1}^{X} \tau_0^i \exp\left(-\frac{t}{\lambda_i}\right) \tag{4}$$

In the measurement, 3rd order approximation (X=3) was employed. λ was thus obtained, and the effects of temperature on λ was derived in the same manner applied to the viscosity as shown in Eq. (2).

$$\log_{10}\lambda = \alpha + \frac{\beta}{T_m+273} + \frac{\varepsilon}{(T_m+273)^2} \tag{5}$$

From the measurements of λ, it was found that the values of coefficients β and ε were very close to those obtained by the viscosity measurements. Thus, the values shown in Table 2 were applied to Eq. (3). During the experiment, λ at the temperature of T_m=20°C of each working fluid was measured in advance. λ of the experiment was then calculated on the basis of the characteristic temperature of the experiment, which was defined as the average value of the inlet and outlet bulk mean temperatures. Table 3 shows the example of λ of different temperatures.

Table 3: Relaxation time of 64.4wt% PAAm solution at various temperatures.

Temperature T_m [°C]	15	20	30	40
Relaxation time λ [s]	6.81	5.32	3.16	2.10

The specific heat capacity at constant pressure c_p, the thermal conductivity k, and the density ρ of the solutions were referred to the values measured by Gucker et al. [11] and Werner et al. [12].

3. Results and Discussion

Figure 2 shows the distributions of the spatially averaged and time mean Nusselt number, Nu_m, distributions in relation to Reynolds number *Re* and Weissenberg number *Wi*. The solid line presents the numerical results of Newtonian fluid flow in a straight channel with square cross section in laminar flow regime [7, 8]. The results of solutions with different viscoelastic properties are compared in the figure. Namely, the descriptions (57)-(64) shown in the legends present the sucrose concentration of each solution as described also in Table 2. Nu_m averaged in the area between the 21st and 30th curve units (N21-30) is plotted in the figure. As will

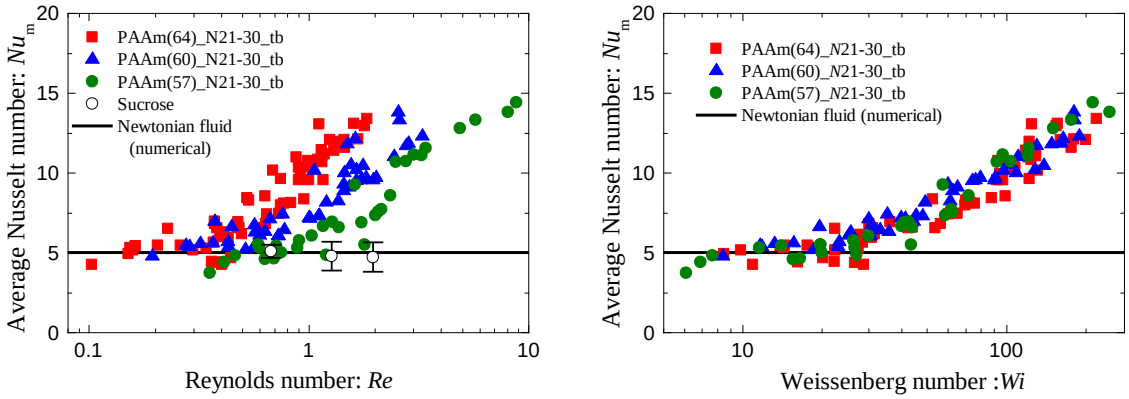

(a) Re vs Nu_m in top/bottom walls heated case (b) Wi vs Nu_m in top/bottom walls heated case

Figure 2: Distributions of locally averaged Nusselt number Nu_m in relation to (a) Reynolds number and (b) Weissenberg number. Nu is averaged in the area between the 21st curve and 30th curve (N21-30) in the case of the top-bottom walls heated. Descriptions (57)-(64) of PAAm cases show the sucrose concentration of the solution.

discussed shortly, the flow and heat transfer characteristics varies depending on the streamwise location and Wi. Among these results, Nu converged to a relatively constant value in the area downstream of the 22nd curve unit (N22) which is considered to be the developed region of each Wi. The influences of the viscoelasticity of the fluid is, therefore, discussed in this region. First, the results of the sucrose solution is constant independent to Re and Wi, and corresponds well with the solid line. This shows the validity of the present measurements.

In the PAAm solution case, Nu corresponds to the sucrose solution case in the low Re regions. In this region, the effect of the viscoelasticity of the fluid is small and the flow is steady and no noticeable vortex structure appears showing a similar flow pattern with those of Newtonian fluids. As Re increases, the flow becomes unsteady and secondary flows are generated which increase the Nu_m. It is clearly shown in Fig. 2 (a) that the Re at which the Nu_m starts to increase differs among the cases of PAAm(57)-(64).

On the other hand, the distributions of PAAm(57)-(64) correlate well with Wi. Wi represents several viscoelastic features of the fluid and flow. One of them is the normal stress differences. The authors has shown that the longitudinal vortices like secondary flows generated in the serpentine channel is mainly attributed to the normal stress differences produced in the area adjacent to the top and bottom walls of the channel [7, 8]. In combination with the curvature of the channel, a force is produced near the walls to drive the fluid toward the center of the curvature. The good correlation between the Nu_m and Wi implies that in the developed region also, the heat transfer enhancement is due to the generation of the secondary flows.

Figure 3 shows the Nu_m distributions in relation to Re and Wi in the cases of PAAm(64). Nu shown here are the averaged values of the three sections dividing the channel in the streamwise as the 1-10th, 11-20th and 21-30th curve units. The legend of these areas are shown as N1-10, N11-20 and N21-30 in the figure. Based on the heat transfer characteristics, these areas represent the entrance, transition and developed regions, respectively. Figs. (a) and (b) show the results in the case of the top and bottom walls heated, while (c) and (d) show the cases of the sidewalls heated.

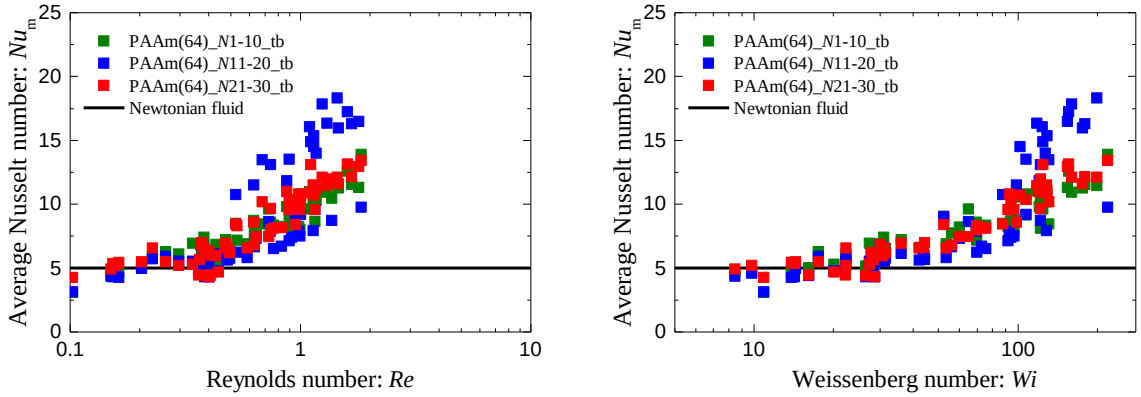

(a) *Re* vs Nu_m in top/bottom walls heated case

(b) *Wi* vs Nu_m in top/bottom walls heated case

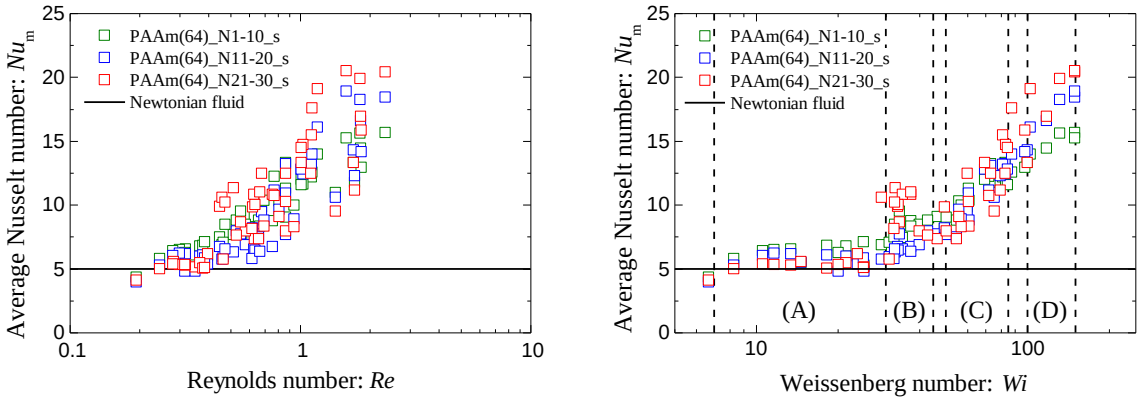

(c) *Re* vs Nu_m in sidewall heated case

(d) *Wi* vs Nu_m in sidewall heated case

Figure 3: Distributions of locally averaged Nusselt number Nu_m in relation to Reynolds number and Weissenberg number. Comparison is made for different streamwise regions of the channel. (a) and (b) are the results of top/bottom walls heated case, and (c) and (d) are the sidewall heated case. Descriptions N1-10, N11-20, N21-30 present the serial numbers of the curve unites in the area of which *Nu* is averaged to obtain each Nu_m.

Under the low *Re* conditions, Nu_m of PAAm cases matches with the solid line showing that the flow structure is similar to that of the Newtonian fluid flow across the whole channel. As *Re* increases Nu_m starts to increase as was observed in Fig. 2. However, in this case, the *Re* in which Nu_m starts to increase are of a same value in the three regions. This shows that the flow becomes unsteady and vortex generation occurs nearly simultaneously in the streamwise direction. Comparing the distributions in relation to *Re* and *Wi* in both wall heated case, the plots are correlated better with *Wi* in which the variation is relatively small. The distribution, however, does not increase monotonically, but shows a characteristic pattern in relation to the streamwise position and *Wi* particularly in the Nu_m distribution of the sidewall heated case. Considering the visualization results also, the heat transfer characteristics can be roughly divided into several regions which are shown in Fig. 2 (d) as (A), (B), (C) and (D).

In region (A), as mention in above, the flow structure is nearly the same with the Newtonian

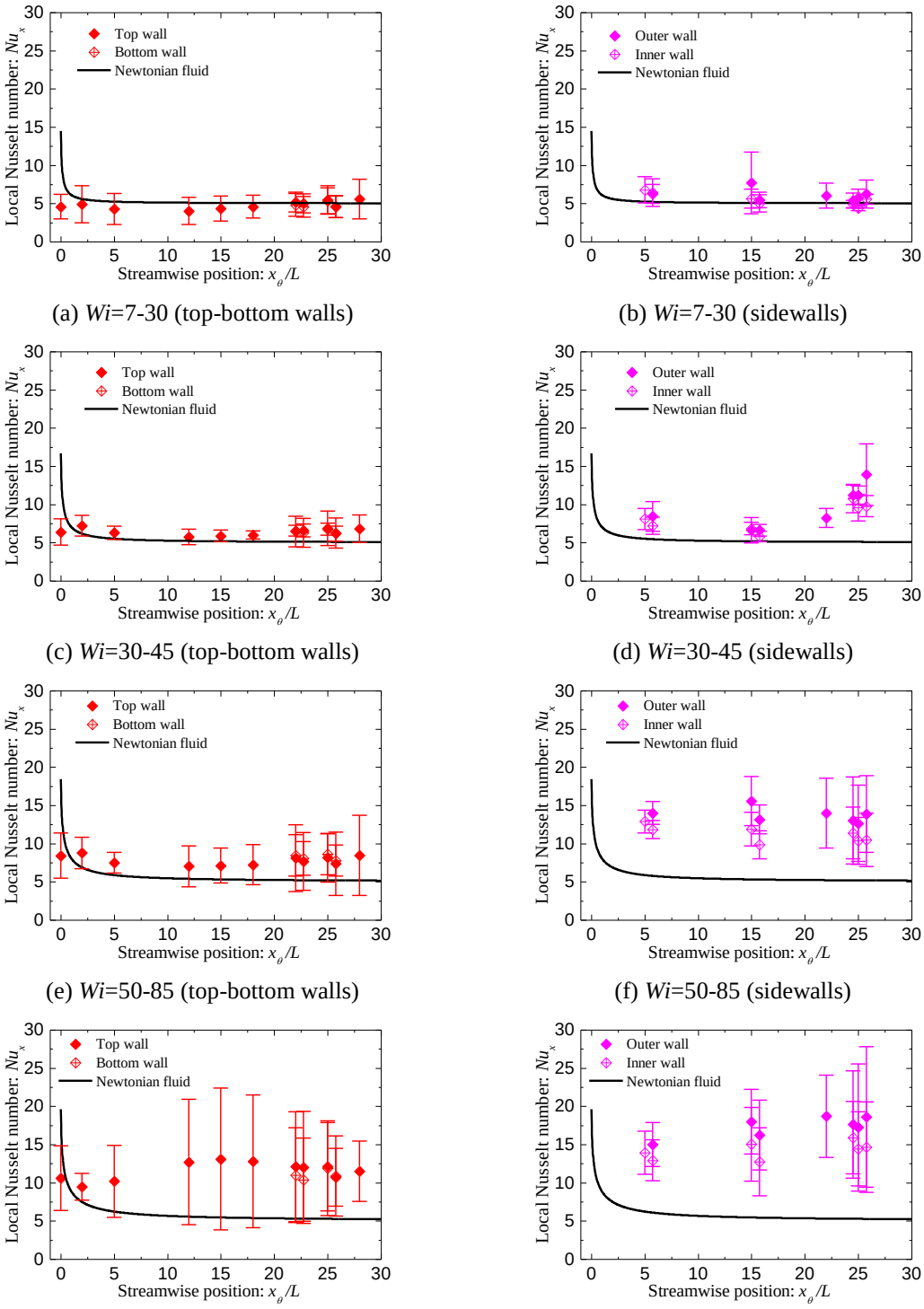

(a) *Wi*=7-30 (top-bottom walls)

(b) *Wi*=7-30 (sidewalls)

(c) *Wi*=30-45 (top-bottom walls)

(d) *Wi*=30-45 (sidewalls)

(e) *Wi*=50-85 (top-bottom walls)

(f) *Wi*=50-85 (sidewalls)

(g) *Wi*=100-150 (top-bottom walls)

(h) *Wi*=100-150 (sidewalls)

Figure 4: Local Nusselt number Nu_x distributions along the streamwise direction. x_θ is the streamwise location along the curved channel and L is the length of one periodical unit. Left side column shows the results of the top-bottom walls heated case, and the filled and outlined symbols show the Nu_x measured at the top and bottom walls, respectively. The right side column are of the sidewall heated case with the filled and outlined symbols presenting the Nu_x measured at the outer and inner side of the curves.

channel. Comparing Fig. 3 (b) and (c), Nu_m increases in the sidewall heated case while Nu_m slightly decreases in the top-bottom walls heated case. Further, a noticeable peak appears in the N21-30 region of the sidewall heated case.

In this *Wi* region, a pair of longitudinal vortices like secondary flows are generated in the channel. This secondary flow generation is attributed to the normal stress difference of the viscoelastic fluid. Due to the shear stress of the main flow generated near the walls and the curvature of the channel, the streamwise (circumferential) component of the stress, $\tau_{\theta\theta}$, produce a driving force to the fluid to flow toward the center of the curvature[6, 7]. In the curved part of channel, the secondary flows convects the fluid located at the channel center toward the outer wall. On the other hand, the fluid located adjacent to the outer wall is driven toward the top-bottom walls. Therefore, the heat transfer at the sidewalls is enhanced while the Nu_m at the top-bottom walls decrease. These secondary flow is fully developed at the downstream side of the channel, and, thus, a marked increase of Nu_m is observed in Fig. 3 (d).

In region (C), the pair of vortices mentioned in the previous paragraph develops to a single vortex. The vortices in this region becomes unstable, and one of the two vortices increases its size and occupy a large portion of the cross section. Further, the main flow, the region of which the streamwise velocity becomes maximum in the cross section, located near the center of this larger secondary flow. Therefore the main flow drifts toward one side of the top-bottom walls, and enhances the heat transfer there.

In region (D), a pair of vortices appears again from the downstream of the channel. As *Wi* increases, the normal stress described in the discussion of region (B) increases. This makes the pair of vortices become more stable, and thus the single vortex like secondary flow and the drift of the main flow decays. Therefore, the sidewall heat transfer enhances markedly and shows a much greater value compared to the heat transfer at the top-bottom walls, particularly in the N21-30 region.

Figure 4 shows the local Nusselt number of each streamwise location Nu_x in the cases of top-bottom walls and sidewalls heated, respectively. Nu_x of the top and bottom walls, and the outer and inner sidewalls of the curve are plotted, respectively. x_θ is the streamwise location measured along the serpentine channel and L is the length of one periodical unit. Distributions of four *Wi* conditions are shown, which correspond to the (A)-(D) regions shown in Fig. 4.

In Figs. 4 (a) and (b), Nu_x is the same with the Newtonian fluid case. In this case, the flow remains steady in all position of the channel. As *Wi* increases, Nu_x starts to increase from the downstream of the channel. Particularly, Nu_x shows a considerable increase at the sidewalls as shown in Fig. (d). This is the reason why a peak was observed in Fig. 3. (d) in region (B). As mentioned before, in this region, a pair of vortices like secondary flow is generated due to the normal stress differences of the viscoelastic fluid. Further, as shown in the figure, the secondary flow starts to develop from the downstream of the channel.

In Fig. 4 (e) and (f), Nu_x increases especially at the sidewalls and the range of the error bars enlarges. It should be noted that the error bars does not mainly present the uncertainty of the measurement method. It is more likely due to the drift of the flow toward one side of the top-bottom walls or the sidewalls. The flow is strongly unsteady for a relatively large time period which will be discusses shortly in the discussion of the visualization.

In Figs. (g) and (h), the error bars increases markedly in both walls. The error bars are large especially in the middle of the streamwise direction in the top-bottom walls cases (Fig. (g)). In this region, the generation of single vortex and the drift of the main flow are significant. Heat transfer coefficient of one side of the top and bottom walls increases while the heat transfer deteriorate at the other side. Thus depending on the experiment, the heat transfer shows a large variation.

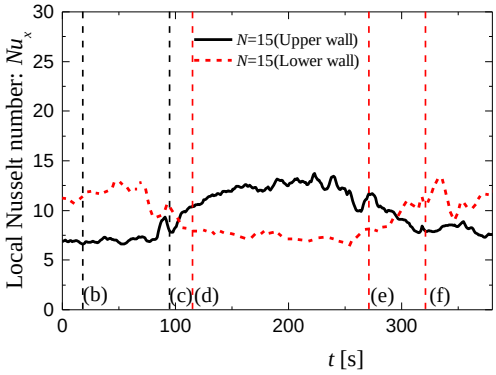

(a) Time distribution of Nu_x at N=15

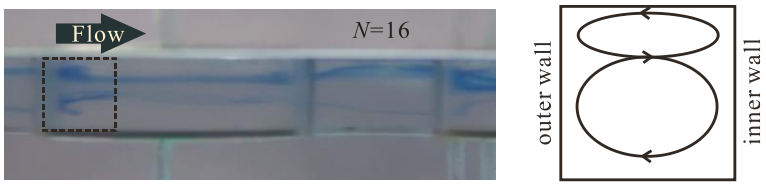

(b) t=18s

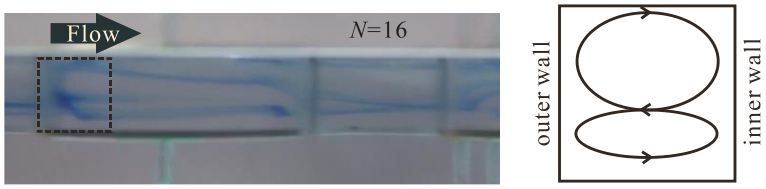

(c) t=95s

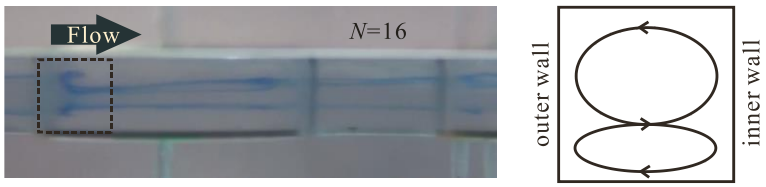

(d) t=115s

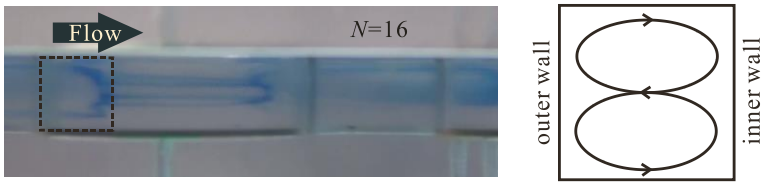

(e) t=271s

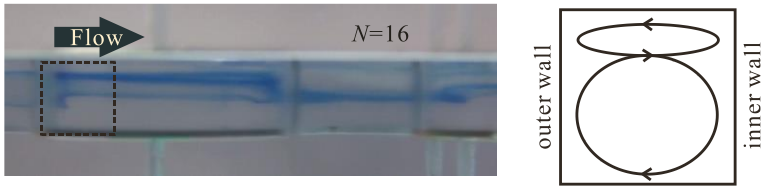

(f) t=321s

Figure 5: (a) Time distributions of the local *Nu* of the top and bottom walls measured at the 15th curve (N15). (b)-(f) the snapshots of the dye visualizing the streak lines of the flow in the area between the 15th and 16th curves (N15-N16). (a) and (b)-(f) were measured simultaneously, and the moments the photos are taken corresponds to the vertical dash lines shown in (a). The flow conditions are *Re*=0.82 and *Wi*=92.

the channel compared with the middle region as shown in Fig. (g). On the other hand, Nu_x increase at the sidewalls. As discussed in Fig. 3, the amplitude of the pair of vortices increases due to the increase of the normal stress differences, and the vortices becomes symmetric. In this case, the heat transfer of the top-bottom walls decreases due to the decay of the drift of the main flow. On the other hand, the sidewall heat transfer increases attributed to the flow convected toward the outer walls. The flow is still unsteady and the flow fluctuate mainly owing to the variation of the vortices size and its position. Since only one thermocouple is attached to each wall, a slight change of the position at which the flow impinges accompanies different Nu_x. Therefore, although the drift of the main flow is not as large as the one observed in the single vortex-like secondary flow case, a certain variation of the average heat transfer coefficient appears in the high *Wi* condition case, too.

Figure 5 shows the time distribution of Nu_x and the visualization results using the dye. The two distributions in Fig. 5 (a) are the Nux measured at the top and bottom walls at the 15th curve unit. The *Re* and *Wi* condition of the measurement are *Re*=0.82 and *Wi*=92 , respectively. Figs. (b)-(f) are snapshots of the streak lines visualized by the dye and viewed from the sidewall. The 15th and 16th curves are shown in the photographs. The dash lines with the labels (b)-(f) shown in Fig. (a) correspond to the period when the snapshots shown in Figs. (b)-(f) are taken.

As shown in Fig. 5 (a), Nu_x fluctuate with time having a relatively long cycle of approximately 200s. The *Wi* of this case is in region between (C) and (D) introduced in Fig. 3 and 4. And the N15 curve is located at x_0/L=15. Under this condition, a single vortex-like secondary flow is generated and the main flow drifts toward the top or bottom wall. The increase of Nu_x at the top or bottom wall and the decrease at the other wall shows the effects of the drift on the heat transfer. The change of the walls at which Nu_x increases indicates that the main flow changes its position to the area closer to the top and bottom walls by time.

To see the structure of the secondary flow and the position of the main flow in the cross section, we now focus on the flow at the cross section near the inflection point which is shown in Figs. (b)-(f) the square drawn by the dashed lines. The streak lines clearly show the two vortices generated and changing their size with time. The schematics of these vortices and their direction are illustrated in right hand side figures. The directions and side of the vortices were estimated by observing the movement of the streak lines in the movie.

The main flow is expected to flow at the positon close to the center of the larger vortex. In this case, the locations of the main flow drift are (b) bottom wall, (c)-(e) top wall, and (f) bottom wall, respectively. This corresponds to which side Nu_x increases confirming the mechanism of the heat transfer enhancement under this *Wi* condition. It is interesting that the direction of the vortices are the same in the two cases having the main flow located close to the top and bottom walls. On the other hand, the vortices turns to the opposite direction when the main flow drifts from one side to the opposite side. This is believed to be due to the fact that when the vortex drifts from one side to the other side it interrupts the secondary flow flowing toward the sidewall. In this case, the flow at the inflection point will flow from the outer sidewall of the upstream curve to the outer sidewall of the downstream curve. This flow will produce an apparent vortices with opposite direction. The detail of the transition of the main flow is, however, still not clear, and further measurement is planned as future work.

4. Conclusions

Heat transfer and flow characteristics of viscoelastic fluid in serpentine channel were measured. In the measurement applying fluids with different properties, the Nusselt number averaged over either the top or bottom walls showed a good correlation with the Weissenberg number *Wi*

while the distributions dispersed largely in relation to Reynolds number *Re*. This was due to the fact that the heat transfer enhancement was mainly attributed to the vortex generation, the amplitude of which can be evaluated by *Wi*.

The local heat transfer distribution and the flow visualization results showed that the flow structure and related heat transfer characteristics in the transition and developed regions can be divided into four regions in the case of the examined range of the present study. As *Wi* increased a pair of longitudinal vortices is generated which enhance the heat transfer at the sidewalls. When *Wi* further increased, the vortices develop to a single vortex and the main flow drifts toward either top or bottom walls. The heat transfer at the top and bottom walls increases in this case. In the developed region, a pair of vortices is generated again from the downstream due to the increase of the normal stress differences. Heat transfer enhanced markedly at the sidewalls in this case.

Acknowledgements

This work was supported by JSPS KAKENHI Grant Number 24360080 and 25630066.

References

1. J. P. Hartnett and M. Kostic. Heat Transfer of a Viscoelastic Fluid in Laminar Flow through a Rectangular Channel. *Int. J. Heat and Mass Transfer*, 28: 1147-1155, 1985.
2. X. Chunbo and J.P. Hartnett. Influence of Rheology on Laminar Heat Transfer to Viscoelastic Fluids in a Rectangular Channel. *Ind. Eng. Chem. Res.*, 31: 727-732, 1992.
3. A. Groisman and V. Steinberg. Efficient Mixing at Low Reynolds Numbers Using Polymer Additives. Nature, 410: 905-908, 2001.
4. R.J. Poole, A. Lindner, M.A. Alves. Viscoelastic Secondary Flows in Serpentine Channels. *J. Non-Newtonian Fluid Mechanics*, 201: 10-16, 2013.
5. S. Tamano, M. Itoh, M. Sasakawa and K. Yokota. PIV Measurement of Secondary Flow in Curvilinear Pipe Flow of Polymer Solution. *Transactions of the JSME*, ser. B. 75: 2115-2121, 2009.
6. J. Zilz, R. J. Poole, M. A. Alves, D. Bartolo, B. Levache and A. Lindner. Geometric Scaling of a Purely Elastic Flow Instability in Serpentine Channels. *J. Fluid Mech*., 712: 203-218, 2012.
7. K. Tatsumi, W. Nagasaka, O. Nakajima, C. L. Heong, and K. Nakabe. Flow and Heat Transfer Characteristics of Viscoelastic Fluid Flow in a Serpentine Channel. *Transactions of the JSME*, ser. B. 79: 93-103, 2013.
8. K. Tatsumi, W. Nagasaka, T. Matsuo and K. Nakabe, A Numerical and Experimental Study on Flow and Heat Transfer Characteristics of Viscoelastic Fluid Flow in a Serpentine Channel. In *Fifteenth International Heat Transfer Conference*, IHTC15-9615, 2014.
9. W. F. Busse, Mechanical Structures in Polymer Melts. II. Roles of Entanglements in Viscosity and Elastic Turbulence, *Polymer Science PartA-2*, 5: 1261-1281, 1967.
10. B. N. Mirsa, Y. P. and Varshni. Viscosity-Temperature Relation for Solution. *J. Chem. Eng. Data*, 6: 194-196, 1961.
11. F. T. Gucker Jr. and F. D. Ayres. The Specific Heat of Aqueous Sucrose Solutions at 20°C and 25°C and the Apparent Molal Heat Capacity of Non-Electrolytes. *J. American Chem. Society*, 59: 447-452, 1937.
12. M. Werner, A. Baars, F. Werner, C. Eder and A. Delgado. Thermal Conductivity of Aqueous Sugar Solutions Under High Pressure. *Int. J. Thermophysics*, 28: 1161-1180, 2007.
13. A. R. Chandrupatla and V. M. K. Sastri. Laminar Forced Convection Heat Transfer of a Non-Newtonian Fluid in a Square Duct, *Int. J. Heat Mass Transfer*, 20: 1315-1324, 1977.
14. W. N. Kays and M. E. Crawford. Convective Heat and Mass Transfer, Second Edition, New York:

McGraw-Hill: 275-287, 1980.

15. W. Kozicki, C. H. Chou and C. Tiu, Non-Newtonian Flow in Ducts of Arbitrary Cross-Sectional Shape, *Chemical Engineering Science*, 21: 665-679, 1966.